Through-Thickness Modulus Gradient and Pattern Fidelity of UV-Cured Thiol-Acrylate Films

Amir Darabi, Lewis M. Cox

Through Thickness Modulus Gradient and Pattern Fidelity of UV-Cured Thiol-Acrylate Films

*Amir Darabi and Lewis M. Cox**

Department of Mechanical & Industrial Engineering, Montana State University, 220 Roberts Hall, Bozeman, MT, 59717, USA

KEYWORDS: Photopolymerization, thiol-acrylate, pattern fidelity, modulus gradients, oxygen inhibition

ABSTRACT: The utilization of photopolymers in diverse applications such as microfluidic devices, gas inhibitors, and biomimetic tissues has surged due to advancements in digital light processing technologies that now support multi-material platforms, facilitating micrometer-scale control over material heterogeneity. However, significant knowledge gaps remain in our understanding of spatiotemporal evolution within these multi-material actinic films and layers. To help bridge these gaps, a thiol-acrylate system is employed for photopatterning, and atomic force microscopy is leveraged to map through-thickness modulus profiles at various UV exposure levels, both in flood and masked curing setups. This approach enables the evolution of material properties to be tracked through the film thickness for incremental light exposure durations, and across different photopatterned feature sizes. The results illustrate complicated modulus profiles that

highlight the complex interplay between light exposure parameters, polymerization kinetics, oxygen inhibition, and light scattering.

1. Introduction

Photopolymers are increasingly utilized across diverse applications including the fabrication of microfluidic devices, gas inhibitors, and biomimetic tissues.[1–4] This surge in usage can be attributed to a shift in digital light processing (DLP) technologies from single-material printing paradigms to the emergent multi-material platforms that provide micrometer and potentially submicron control over heterogeneity.[5–9] DLP processes photopolymers by building objects layer by layer, enabling the manipulation of mechanical properties through controlled light exposure.[3,10] An ongoing challenge in layer by layer printing is the uncertainty over material properties through the thickness of a single printed layer. Despite the expansive literature into the kinetics of photopolymerization,[11–14] significant gaps remain in our understanding of spatiotemporal evolution within heterogeneous photopatterned layers.

Local material characteristics in photopolymer systems are influenced by the degree of polymerization. In network forming resins, progressing monomer conversion is associated with higher crosslink densities, and increasing elastic modulus.[15–20] If the mechanical properties of a cured actinic resin are a function of the total energy dose (the product of intensity and duration) only, then the system is considered reciprocal and material properties, along with degree and depth of curing, are readily predictable.[21,22] This phenomenon is captured in ‘working curve’ models, which predict cure depth based on light exposure parameters.[23–26] In general, these models predict

that the crosslink density in a light-exposed region diminishes over the thickness of polymer films, yielding inferior mechanical properties towards the far end.

However, there are practical limitations to reciprocity law and covariates such as oxygen inhibition, photobleaching, and heat generation undermine its predictions.[21,27–29] Additionally, in single-film processing applications, use of a photomask can impart additional complexities in material heterogeneity.[30] A thorough investigation into the through-thickness modulus variations in photopolymer films remains outstanding, and such studies are crucial for controlling material heterogeneity at different scales.

This research focuses on a thiol-acrylate photopolymer system, exploring the orthogonal reactions that drive its polymerization. An initial Michael addition click reaction provides a rubbery network,[31] and subsequent radical-mediated acrylate homopolymerization is characterized *via* atomic force microscopy (AFM) through the film thickness. AFM modulus maps are collected at several UV exposure durations to spatially resolve network evolution from a rubbery state, through the leathery transition regime, and into a glassy state. Both flood and masked curing setups are employed, and consideration is given to the length scale of masked features. The insights gained here will further our ability to precisely engineer the mechanical behavior of photopolymers in technologically relevant applications.

2. Materials and Methods

Materials: Pentaerythritol tetrakis(3-mercaptopropionate) (PETMP), trimethylolpropane triacrylate (TMPTA), 2,2-Dimethoxy-2- phenylacetophenone (DMPA), triethylamine (TEA), and butylated hydroxytoluene (BHT) are procured from Sigma-Aldrich. The chemical structure of chemicals are shown in Figure S1 in supporting information.

Film processing: An off-stoichiometric ratio of 1:2.75 is selected between the thiol (PETMP) and acrylate (TMPTA) functional groups, with excess acrylates. TEA (0.1 wt%) is added as the catalyst and DMPA (1.5 wt%) is added as the photoinitiator. Trace amount of BHT (0.05 wt%) is added as inhibitor to improve the shelf life of the polymer. All chemicals were purchased through Sigma Aldrich. The first polymerization process, initiated upon mixture, is a step growth Michael addition "click" reaction between thiol and acrylate monomers. The solution is cast on large glass slides (4" by 5") and allowed to reach full conversion overnight. To ensure uniform thickness, shim stock sheets of known thickness are placed on the glass slides as spacers (see Figure S1 in supporting information). The result is a rubbery polymer film with excess unreacted acrylate functional groups and an average thickness of 100μm ± 6μm across all synthesized polymer films. Therefore, the slight variations in film thickness are neglected in this work.

The "top" surface of the rubbery film is then laminated by hand against a soda lime superstrate photomask, with etched-chrome patterns. This is accomplished by bringing one edge of the sample surface into contact with the photomask and then allowing that contact region to spread outward as the sample is gently "rolled" onto the mask. A visual inspection is then performed to ensure no obvious air bubbles have been trapped between the mask and sample. The treatment of the bottom surface in this manuscript is noteworthy. To mitigate light reflection back into samples, index matching oils and neutral density filters are commonly applied along the "bottom" of samples in curing setups. However, these oils were observed to contaminate sample surfaces and frustrate AFM characterization. To preserve the cleanliness of surfaces, an index-matching, rubbery cover film is made from a 1:1 stoichiometric ratio of PETMP and TMPTA and rolled against the bottom surface using the previously described lamination technique. For context, an additional benefit of using index matching oils and neutral density filters is mitigation of oxygen inhibition during the

curing process. The diffusivity of oxygen in the present material system is not explicitly measured but can be approximated from other thiol-ene rubbers in literature (see Section 3 in supporting information). While orders of magnitude lower than PDMS (commonly used in DLP processes), the diffusivity of oxygen through the index-matching cover film used as a substrate in this study is much higher than that of the soda lime photomask and traditional neutral density filters. Accordingly, the substrate may act as a limited reservoir for the diffusion of molecular oxygen into the sample during curing. The potential impacts of this boundary condition are discussed in Section 3.1. The configuration of the described material stack is depicted in Figure 1A. The stack is then positioned above a black felt box prior to illumination.

Upon exposure to ultraviolet (UV) light (OmniCure S1500 lamp, 300 nm – 400 nm wavelength filter, 30 mW/cm^2), the photoinitiator generates free radicals that initiate the homopolymerization of excess acrylates in the polymer network, increasing the crosslinking density and elastic modulus in illuminated regions, Figure 1B.[32] UV exposure time is set to 0.5, 1, 3, 10, 30, and 300 sec, translating to energy doses of 15, 30, 90, 300, 900, and 9000 mJ/cm^2, respectively. Four different feature widths of 10, 20, 50, 100 μm are photopatterned on polymer films. The UV light is subsequently absorbed by a box filled with black felt (see Figure S1 in supporting information).

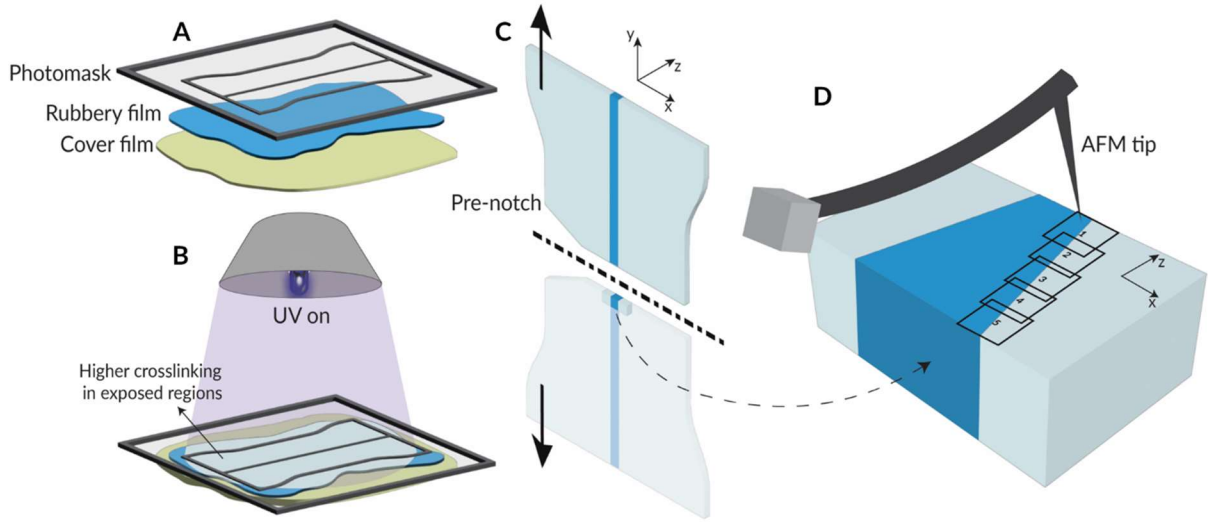

Figure 1. A) Schematic of the UV curing setup where the rubbery film is laminated between the superstrate photomask (top) and the substrate cover film (bottom). B) The rubbery film begins the transition to a glassy state upon UV exposure. C) Pre-notched photopatterned film is fractured along the patterned line to achieve a smooth cross section. D) Film's cross section is scanned using AFM with several overlapping scans for subsequent stitching to achieve a through-thickness modulus map.

Tensile testing: Polymer films are patterned with three different interlayer geometries, consisting of one flat line and two sinusoidal geometries with amplitudes of 2 and 5 mm, and a constant wavelength of 1.4 mm. Each geometry is patterned at four different interlayer widths of 10, 20, 50, and 100 μm. The composite films have a dog bone outline with a 15 mm length, 9 mm width at the ends, and 7 mm width at the middle of the specimens. Photopatterned films are subject to 2% strain ramp using dynamic mechanical analysis (DMA, Q800, TA instruments) to measure the

modulus of photopatterned composites across different linewidths and patterns, with five replicates per group.

Atomic force microscopy: To obtain sufficiently flat cross sections, a pre notch was placed on the edge of the dog-bone samples (Figure 1C), which were subsequently stretched until failure. Fractured samples were taped to 90° sample mount for imaging. Prior to modulus mapping, optical microscopy followed by topographic tapping mode scans were used to identify regions of the fracture surface that were both flat, and oriented orthogonally to the surfaces of the dog-bone. A surface roughness on the order of 10's of nm is still observed on these samples of these surfaces. This roughness contains features of similar length scale to the probe tip and introduces a faint artifact into the modulus maps, described in the discussion.

The fractured films are carefully mounted onto a metallic stage, orienting the cross-section upwards, for subsequent characterization using an atomic force microscope (AFM, Asylum Research Cypher S). Modulus maps are obtained through AFM fast force mapping mode using a 300 Hz scanning rate and a 40 N/m tip (Tap300Al-G, BudgetSensors). As shown in Figure 1D, multiple modulus maps are scanned with a small overlap to compile a comprehensive map of modulus variations throughout the thickness of the polymer films.

Fast force mapping is ideally suited for comparing modulus values within a single scan. However, given that the objective of this study is to integrate multiple AFM maps, it becomes crucial to address potential inconsistencies arising from factors such as tip wear and tip contamination. To surmount this challenge, all maps associated with a single specimen are collected on the same day without removing the tip cantilever, using a consistent indentation force across multiple scans. An indentation force of 500 nN was selected due to its suitability for measuring both rubbery and glassy surfaces. This setpoint provides a good signal to noise ratio

and small changes to this value (+/- 50 nN) does not result in significant changes to the measured modulus values of the sample. Calibration scans are conducted on the surface of a fully cured polymer film with similar formulation to track any potential tip wear that rarely occurs after multiple scans.

Processing of modulus maps: To stitch modulus maps acquired from the film's cross-section, we use a custom MATLAB code. This code combines raw data spreadsheets of overlapping AFM maps through user-identification of corresponding points. Stitched maps do not align in a perfectly linear fashion through the film thickness because 1) the work tracks certain interfacial features laterally and 2) small amounts of lateral drift are generally unavoidable. The final, stitched dataset is used to plot the through thickness modulus map of the film. Some challenges that may question the reliability of modulus maps arise when scanning regions close to the cross-sectional edges. These challenges are further discussed in *Section 3.1*.

3. Results and Discussion

3.1 Evolution of modulus profiles during flood exposure

Rubbery films were flood cured with UV at incremental exposure times, fractured to expose the cross-section, and then imaged using AFM fast force mapping to quantify modulus variations through the thickness. Imaging the outermost edges of the cross-sectioned film presents two concerns; 1) the Hertzian contact model used to interpret force curves assumes an infinite substrate, and the presence of an edge impinging on the volume actuated by the AFM probe undermines this assumption in unknown ways, and 2) significant aggregations of dust and debris often occluded these regions of the surface (see Figure S2 in supporting information). Accordingly, presented modulus maps exclude the upper and lower 5 μm of the sample thickness, and modulus values at

the edges are collected from the two film surfaces directly. During irradiation, the "top" side of every film was laminated against a transparent soda lime plate and the "bottom" side was laminated against a cover film.

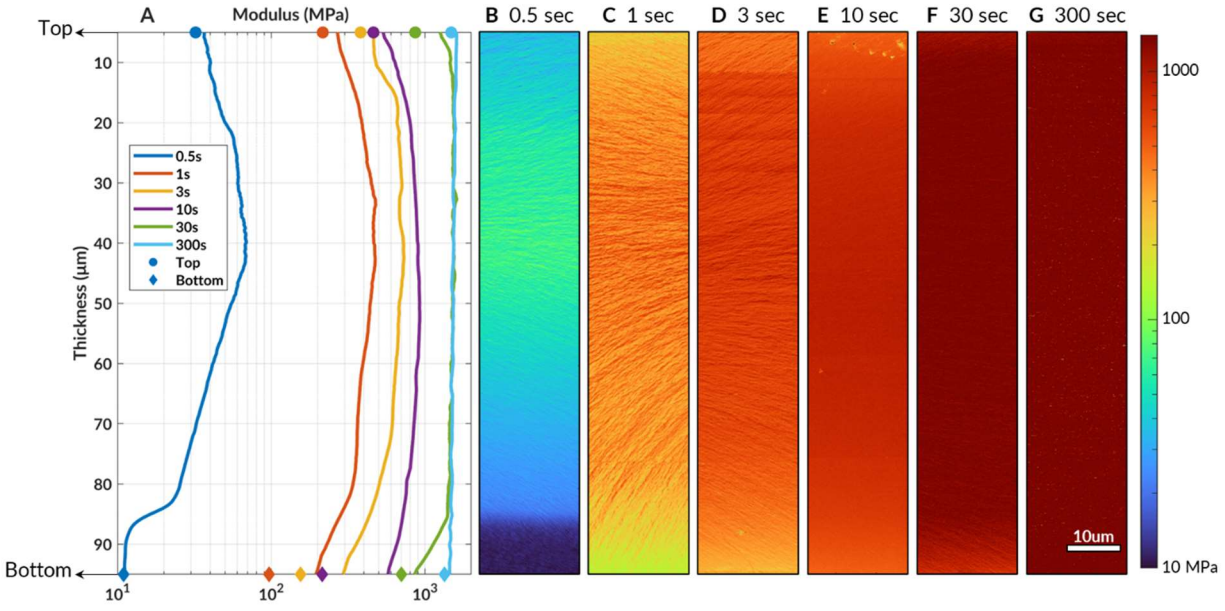

Figure 2. Through thickness modulus gradient of flood cured polymer films represented as A) log-scale mean modulus, along with mean modulus of top and bottom surfaces, and B-G) log-scale AFM color maps for 0.5 to 300 sec UV exposures. The presented data illustrates the 5 to 95 µm depth of the film cross section considering the challenges associated with scanning cross-sectional edges.

Figure 2A depicts the evolution of modulus gradients through the films' thickness, accompanied by the moduli measured at the top and bottom surfaces, for six incremental irradiation times of 0.5, 1, 3, 10, 30, and 300 sec. Before discussing the evolution of the through thickness modulus profiles, some observations should be noted. First, horizontal lines in the modulus maps (especially evident in Figure 2D) are artifacts that occasionally appear during AFM scans. Second, the

Hertzian contact mechanics model that is used to calculate sample modulus from force-displacement data assumes the sample surface to be a flat plane. Surface topography and roughness have the potential to introduce artifacts into the modulus maps. In several stitched modulus maps, most strikingly evident in Figure 2C, a feathered texture is discernable as curved, linear features, sub-micrometer in width. It should be noted that these are artifacts which directly correspond to topographic features. Accordingly, the discussion that follows focuses on micrometer, and larger, scale trends in the modulus gradients.

While the cross-sectional scans demonstrate that stiffness increases with exposure time, the modulus profiles contain interesting trends beyond this intuitive observation. For all tested exposure times of 30 sec and less, the modulus near the top and bottom film surfaces are significantly lower than the modulus near the center of the films. The phenomenon is most pronounced at shorter exposure durations. After 0.5 sec of exposure, a modulus of 30 MPa was measured at the top surface, increased until reaching a peak value of 70 MPa at a depth of approximately 45 μm, decreased exponentially to 25 MPa at an approximate depth of 85 μm thickness, then sharply drops to around 10 MPa and remains somewhat consistent for the 15 μm adjacent to the bottom surface. Longer exposure times flatten out this profile, as shown in Table 1 comparing the relative standard deviation (RSD) of each modulus profile. While the 300 sec sample shows excellent modulus uniformity, 30 sec is enough to capture a relatively uniform glassy modulus throughout most of the film, with reductions in modulus observed only within ~10 μm of the top surface and ~15 μm of the bottom surface (RSD = 9.42%). This is a relevant consideration for time sensitive layer-by-layer DLP applications.

Table 1 – Relative standard deviation for each modulus profile.

Exposure duration (sec)	**0.5**	**1**	**3**	**10**	**30**	**300**

$\boldsymbol{RSD = \frac{\sigma_E}{\mu_E} \times 100\ (\%)}$	33.67	19.71	19.22	12.83	9.42	2.62

$\boldsymbol{\sigma_E}$ is the modulus standard deviation and $\boldsymbol{\mu_E}$ is the modulus average.

To understand this data, light intensity as well as the concentration and diffusivity of oxygen and chemical species should be considered, but this endeavor is not trivial. As photopolymerization proceeds, the films evolve from a rubber, across their leathery glass transition regime, to a glass. Throughout this process, coefficients of diffusivity will change by an order of magnitude or more, and the concentrations of oxygen, photoinitiator, and free radicals will experience spatiotemporal complexity.

Specifically, upon UV exposure, DMPA breaks down and introduces free radicals in the network, leading to homopolymerization of excess acrylates and increasing crosslink density. While the specific relationship is complex and dependent on proximity to the material's glass transition regime, modulus has a monotonic relationship with cross-linking density. At early exposure times, when DMPA concentration can be approximated as uniform, the light intensity will decrease as a function of depth, with an approximate 25% drop in intensity at the bottom of the 100 μm film, per Beer-Lambert law (see Figure S3 in supporting information). The corresponding modulus profile would, in the absence of other covariates, monotonically decrease throughout the depth at early time periods in the curing process, but deviations from this trend are clear.

A likely covariate is oxygen, which inhibits free radical polymerization by scavenging radicals and forming peroxy radicals that cannot initiate polymerization immediately.[33,34] The diffusivity of oxygen (D_{O_2}) in this material system is not known but can be approximated from measurements in similar materials (see Section 3 in supporting information).[2,35–39] Employing a simple scaling

relationship ($\tau = \frac{L^2}{D_{O_2}}$) to approximate the diffusion times (τ) and length (L) scales of oxygen indicates that the characteristic time scale for oxygen to diffuse across a 100 μm thick rubbery film falls in a range of $150 < \tau_{rubber}(sec) < 200$ in the initial rubbery film and increase to $2500 < \tau_{glass}(sec) < 3800$ in the fully cured, glassy network. At the shortest, 0.5 sec exposure time, where the material is still predominantly rubbery, this corresponds to a characteristic diffusion length scale of ~5 μm, a value relevant to the observed length scales in the modulus profile associated with deviations from the monotonic trends expected from light absorption, warranting additional discussion.

Prior to UV exposure, polymer films are cast, covered in foil, and given 24 hours for the initial step-growth polymerization to reach full conversion. Throughout the mixing, casting, and curing process, oxygen is expected to diffuse into the samples. During the UV curing process, oxygen can diffuse within the film, scavenging radicals, although the coefficient of diffusion of oxygen drops with increasing crosslink density. The potential for additional oxygen to enter the sample from the top and bottom surfaces is an important consideration. While imperfect sample lamination may trap small amounts of oxygen between the soda lime photomask, visual inspection was used to mitigate this chance, and diffusion across the soda lime plate itself is expected to be negligible across the time scales investigated here.

As mentioned earlier, the increasing modulus profile at the top half of the films, especially at shorter irradiation times of 0.5 and 1 sec, is counterintuitive when compared to the light intensity profile. Although a simple explanation is not apparent, the authors infer that this phenomenon is caused by a competition of light intensity and oxygen diffusion. The concentration of free radicals is highest at the incident surface due to the higher light intensity. The higher the concentration of free radicals, the larger the amounts of oxygen that are consumed, scavenging the free radicals

near the top region. This could lead to an oxygen concentration gradient that cause the oxygen from within the film to diffuse upwards to the top surface. However, this context is necessarily incomplete and requires investigations on spatiotemporal oxygen concentrations within the polymer in masked-based curing techniques.

The cover film at the bottom of the rubbery polymer is a soft material with similar diffusivity to the sample at short irradiation times, and thus, facilitates diffusion of oxygen into the curing sample. This phenomenon, in addition to light attenuation, results in a relatively uniform 10 MPa "dead zone"[40–43] near the bottom of the film after 0.5 sec of exposure in Figure 2A and 2B, where polymerization is almost entirely arrested. Although the modulus profile exhibits a minor gradient in this region, no measurable contrast in modulus relative to the initial film stiffness is observed. Oxygen diffusivity within the network rapidly decreases with longer irradiations, and the stiffness within the dead zone increases measurably after 1 sec of exposure. Even after curing begins, this region consistently exhibits the lowest modulus values for all irradiation times up until full conversion.

Other covariates impacting modulus profiles include gradients in DMPA concentration as well as the moieties resulting from DMPA photolysis, known to cause minor variations in light absorption profiles over time.[44,45] While DMPA consumption is not tracked over time, the achievement of a uniform profile after 300 sec indicates its residual presence, although it is still possible for polymerization to occur without the presence of photoinitiator at high doses.[46] Finally, we note that thiol-ene systems have low susceptibility to UV degradation, and no evidence of degradation is observable in the modulus profile at 300 sec UV-exposure.[47]

3.2 Evolution of modulus profiles during photopatterning of a 10 µm line

Next, we employ a photomask pattern with a 10 μm wide strip of chrome in a transparent field and characterize the evolution of a compliant line in a glassy matrix. A schematic of modulus mapping at the masked/exposed interface, along with modulus profiles of photopatterned films with 0.5, 1, 3, 10, and 30 sec exposure durations, are depicted in Figure 3. Upon illumination, an interface takes shape along the masked and exposed regions, Figure 3B. There are several consistencies between these results and those of the flood cured samples. Specifically, the modulus is lower near the two surfaces and higher in the middle of the exposed region, with a similarly uncured region at the bottom of the film after 0.5 sec of exposure, associated with an oxygen saturated region that inhibits crosslinking events. Eventually, a nearly uniform glassy profile, with drop-offs near the surfaces, is again reached after 30 sec of exposure.

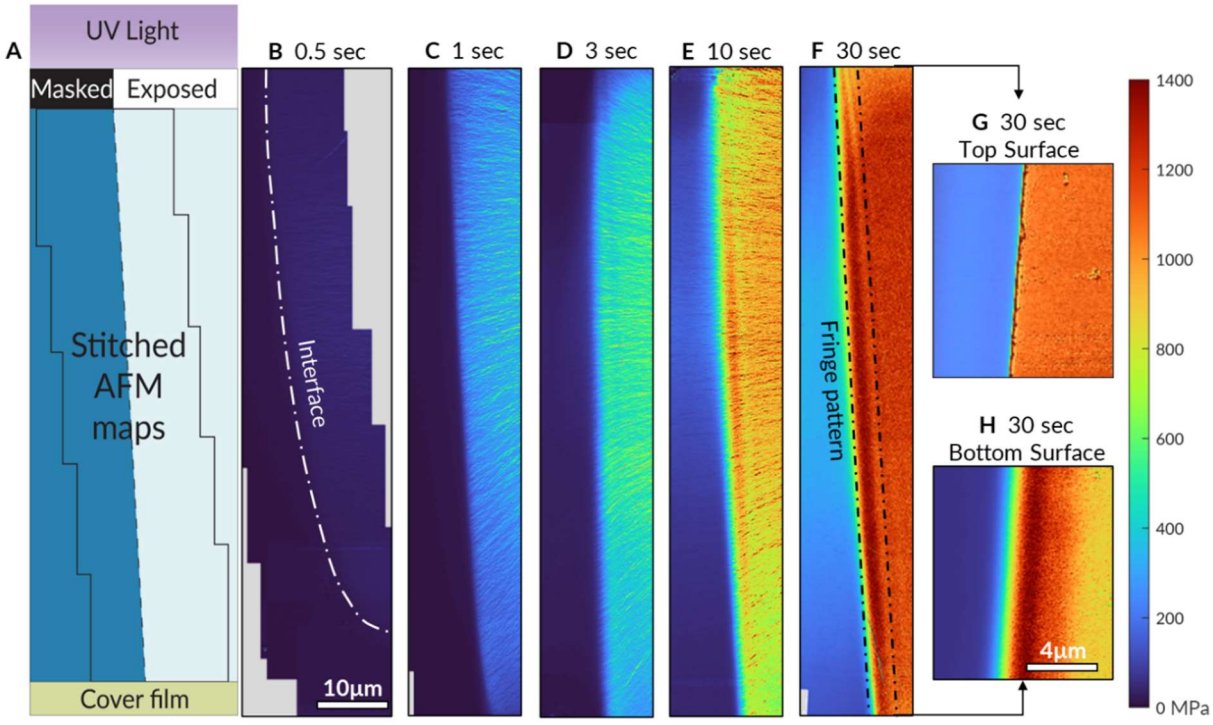

Figure 3. A) A schematic of photopatterned film's cross section and overlapping AFM modulus maps that are stitched together. Masked areas in the superstrate photomask cover the film from incident light and inhibit immediate polymerization. B-F) Through thickness modulus map with

exposure durations of 0.5 to 30 sec. The interface does not extend throughout the film's cross section at 0.5 sec exposure (B). Fringe patterns are formed at the masked/exposed boundary around the 1 sec mark (C) and become more prominent at higher doses (D-F). G) AFM scan from the top surface exhibits a sharp interface between masked and exposed regions, while H) AFM scan from the bottom surface shows the irregularities at the interface due to the expansion of fringe pattern through the thickness.

Below the masked feature's interface, an evolving modulus profile is observed through the thickness of the film. At early exposure times of 0.5 and 1 sec, the boundary exhibits a parabolic shape, indicating that oxygen from the shaded material volumes is diffusing laterally into the exposed regions, inhibiting polymerization. As oxygen inhibition is overcome at higher doses, this boundary evolves into a straight line, tilted around 2 degrees off the vertical axis. Modulus maps of the top and bottom film surfaces indicate that the pattern in material modulus exhibits a 10 μm linewidth on the top surface, consistent with the photomask geometry, and broadens to a thickness of approximately 12 μm at the bottom surface. This feature broadening phenomenon may be attributed to the light scattering and flaring angle of light rays after colliding with the superstrate soda lime glass.

Another consistent phenomenon that appears at 1 sec exposure and becomes more prominent with longer irradiations is the irregular fringe pattern in the modulus profile at the interface between the masked and exposed regions (Figures 3D to 3H). Light diffraction at the edge of the chrome mask and a resulting spatial pattern in light intensity is inferred to be the cause of the local modulus gradients at the interface.[48–50] This hypothesis is supported by the presence of a sharp interface in AFM modulus maps of the top surface (Figure 3G), which develops into a non-uniform

interfacial modulus gradient that broadens as a function of depth through the film, evident on the bottom surface (Figures 3H). It is noteworthy that certain samples contained unintended presence of particulate contaminants that generated similar fringe patterns within the illuminated volume (see Figure S4 in supporting information).

The stability of modulus in the masked regions is critical to a broad range of photopatterning applications. Figure 3 provides clear evidence of curing in masked regions, with a peak modulus of ~300 MPa arising in the middle of the 10 μm feature after 30 sec exposure. The modulus profile in the masked region exhibits minima in proximity to the surfaces and maximum near the center of the film thickness, a similar trend observed in flood cured films (Figure 2). Several factors such as light scattering and reflection, radical diffusion, and oxygen diffusion may contribute to the partial curing of the masked regions. Light reflection from the transparent substrate may contribute to the partial curing. Diffusion of free radicals from the exposed regions into the masked regions is possible at early time scales. However, unintended curing extends several micrometers into the masked region and the characteristic diffusive length scales of radicals are likely significantly smaller than those of oxygen due to differences in the size of the diffusing molecules, so the effects are most likely relegated to sub-micrometer length scales adjacent to the interface. Still, additional investigations are needed to confirm this hypothesis.

3.3 Effect of the linewidth of photopatterned features on through thickness pattern fidelity

In this section, we explore modulus profiles in the masked region for larger feature sizes of 20, 50, and 100 μm and compare them to the 10 μm linewidth. Here, an exposure duration of 30 sec was selected since it results in near-uniformity and is comparable to exposure times and doses used in digital light processing techniques.[10,51,52]

For linewidths of 10, 20, and 50 μm, a non-uniform through-thickness profile is observed, with a maximum value near the center of the films (Figure 4B to 4D), consistent with flood curing results. The peak modulus of the masked feature scales inversely with the feature width. For a 10 μm linewidth, modulus in the masked region increases to a maximum of 300 MPa in the middle (~40 to 60 μm) of the film thickness. This value drops to 160 MPa and 60 MPa for linewidths of 20 μm and 50 μm, respectively. At the largest feature width of 100 μm, the modulus is constant throughout the thickness and equal to the modulus of a rubbery film prior to UV exposure (~ 10 MPa). These trends indicate that the final modulus of the masked regions is largely governed by a competition of unintended dosing and oxygen inhibition. Larger feature sizes provide a larger reservoir of oxygen that will diffuse towards the masked-exposed interface and inhibit spurious polymerization. Smaller feature widths will result in a larger average dose within the masked volume, and consume the oxygen dissolved in the masked regions of the network more rapidly. A scan of a 100 μm feature after 300 sec of exposure (see Figure S4 in supporting information) indicates that overexposure will eventually result in partial curing within these larger features, supporting the interpretation that oxygen inhibition is critical for preservation of pattern fidelity.

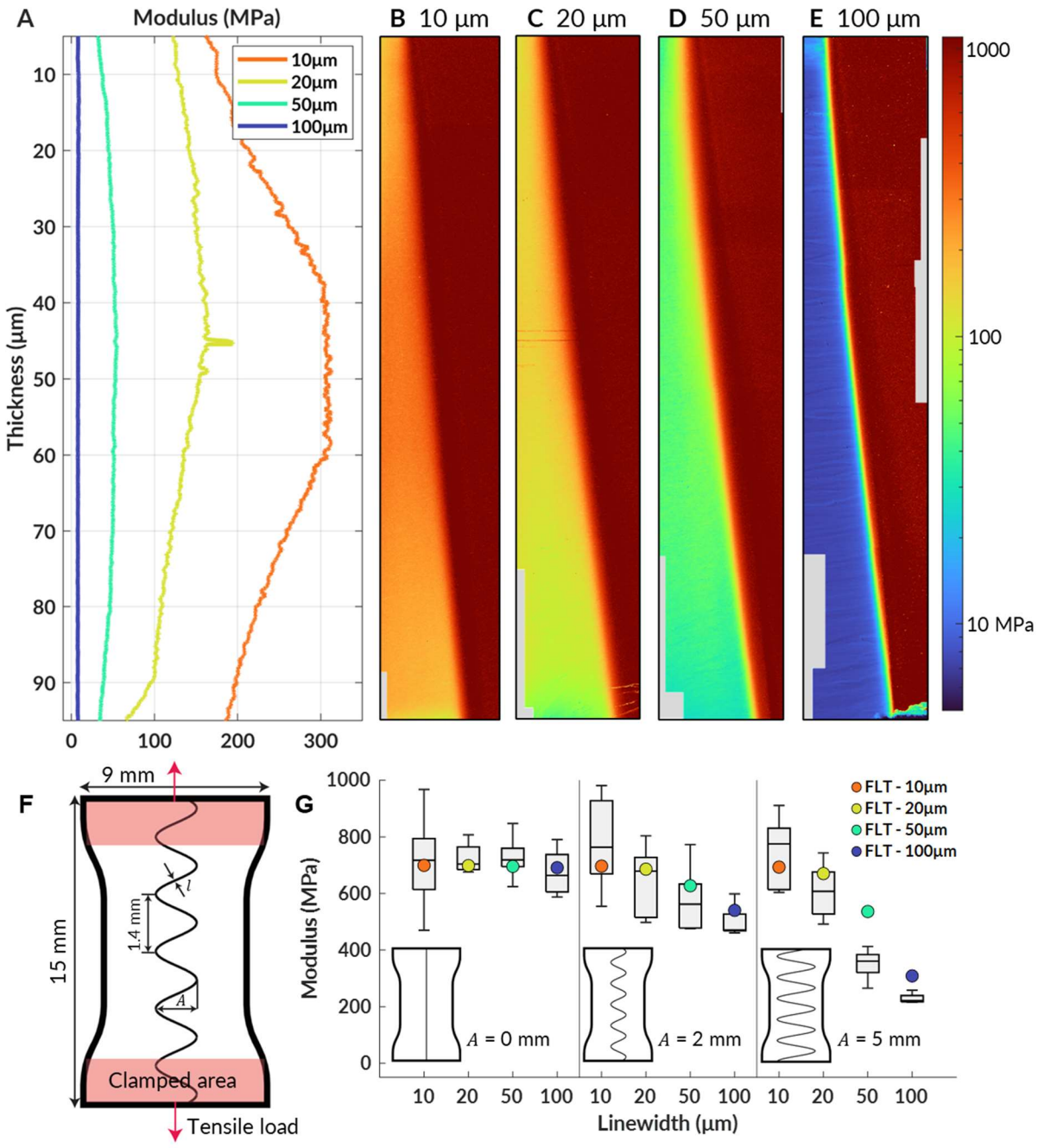

Figure 4. Through thickness modulus gradient for four different feature sizes illustrated as A) mean modulus of the masked region and B-E) log-scale color maps. F) The dog bone sample outline and dimensions. Embedded sine waves have a wavelength of 1.4 mm, with interlayer width (l) and amplitude (A) varying among different groups. It is worth noting that samples are not pre-notched for tensile testing. G) The modulus of composites embedded with various geometries

reported by dynamic mechanical analysis, shown as box plots. Fiber laminate theory (FLT) is used to predict the composite modulus using data obtained from AFM, shown as dots.

3.4 Effect of pattern fidelity on overall mechanical properties

Even if unintended curing is present, interrogating the degree to which it occurs enables better prediction of bulk, composite properties for a given, arbitrary pattern. In a recent study, we examined the geometry-performance relationships of a wavy, compliant interlayer embedded within stiff matrices, but were limited to larger, 100 μm, interlayer widths due to unpredictable partial curing.[53] Following the results displayed in Figure 4A to E, we apply fiber laminate theory (FLT) to anticipate the bulk modulus of composite films in relation to the interlayer's geometric features and compare FLT predictions with experimental data (see Section 5 in supporting information).

Polymer films are photopatterned with three different amplitudes and four different interlayer widths for 30 sec with a light intensity of 30 mW/cm^2. Specifications on interlayer geometries and sample dimensions are shown in Figure 4F. It is worth noting that the films embedded with flat line patterns are similar to polymer films studied earlier. Boxplots in Figure 4G show the modulus values obtained from dynamic mechanical analysis (DMA), with the upper and lower quartiles represented by the box and minimum and maximum values represented by the whiskers. The results indicate that the higher amplitudes exhibit lower moduli for the interlayer width of 100 μm, but the contrast between different geometries diminishes with smaller feature sizes.

To estimate the overall modulus of the composite, FLT requires modulus values of the rubbery and glassy components. The bulk modulus of the glassy polymer is measured with DMA using

flood cured films and used in FLT. However, since measuring the bulk modulus of the partially cured interlayers is not possible, AFM modulus values exhibited in Figure 4A are averaged for each feature size and input in the FLT model (see Section 5 in supporting information). FLT predictions of the composite modulus values are shown as circles in Figure 4G. Although discrepancies between macroscale and nanoscale modulus measurement are acknowledged, FLT results show an excellent ability to predict experimental measurements of bulk composite moduli associated with different interlayer linewidths and waviness.

4. Conclusion

In this study, we investigated the evolution of modulus profiles in UV-cured, non-stoichiometric thiol-acrylate films, employing AFM fast force mapping to elucidate modulus variations through the films' thicknesses at various stages of UV exposure. Modulus profiles were examined in flood cured films, as well as films masked with a line feature of varying widths. Our findings provide new insights into the spatial variability of mechanical properties in these films, highlighting the influence of UV exposure time (and dose), oxygen diffusion, light diffraction, and light reflection on spatiotemporal modulus distributions.

Results revealed that, while modulus generally increases with UV exposure time, non-uniform modulus gradients are readily observed through the thickness of films. Lower moduli are present near the top and bottom surfaces of a film's cross section, and peak modulus values are found near the center. This trend was especially pronounced at shorter exposure times, highlighting a complex interplay between light intensity profiles, oxygen diffusion, and polymerization kinetics. Observed modulus gradients diminish with longer exposure times, leading to a nearly uniform modulus

profile after 30 seconds of exposure with gradients present only near the surfaces. A flat modulus profile is achieved through the thickness after 300 seconds.

Masked line features with widths of 10, 20, 50, and 100 μm were photopatterned into films to create glassy composites with a compliant interlayer, and the fidelity of the compliant lines were characterized. Results show that smaller features exhibit greater degrees of unintended curing underneath the photomask, likely due to reduced availability of oxygen reservoirs to inhibit curing, coupled with increased light dosage. This was in contrast to larger features exhibiting excellent pattern fidelity and minimal spurious curing. The results from through-thickness modulus characterization were integrated into fiber laminate theory, demonstrating that a quantitative understanding of modulus drift in masked features enables successful prediction of bulk composite properties for various interlayer geometries and line widths.

In conclusion, this study provides spatiotemporal characterization of modulus evolution in UV-photopatterned thiol-acrylate films, offering insights that are critical for predicting, and potentially optimizing, photopolymerization processes and the mechanical properties of resulting composites. Future work quantifying the evolution of oxygen and photoinitiator concentration gradients in these systems would address the limitations of this study, and further refine our understanding of actinic polymerization processes.

ASSOCIATED CONTENT

Supporting Information

Supporting information is available free of charge.

A schematic of UV-curing setup, AFM maps from cross sectional edges, light attenuation profile, estimation of oxygen diffusion coefficient, additional through thickness modulus maps, fiber laminate theory details (PDF)

AUTHOR INFORMATION

Corresponding Author

* Lewis M. Cox - E-mail: lewis.cox@montana.edu

Author Contributions

The manuscript was written through contributions of all authors. All authors have given approval to the final version of the manuscript.

A.D: Conceptualization, Methodology, Formal Analysis, Investigation, Data Curation, Visualization, Writing-Review-Editing

L.C: Conceptualization, Methodology, Formal Analysis, Investigation, Visualization, Writing-Review-Editing, Supervision, Project Administration, Funding Acquisition

Notes

The authors declare no conflict of interest.

ACKNOWLEDGMENT

The authors thank Dr. Callie Higgins at the National Institute of Standards and Technology for providing insights on the collected data. We acknowledge funding support from the National

Science Foundation under grant numbers CMMI-2038512 and CMMI-2038505. This work represents the views of the authors and not necessarily those of the sponsors.

REFERENCES

(1) Paul, R.; Zhao, Y.; Coster, D.; Qin, X.; Islam, K.; Wu, Y.; Liu, Y. Rapid Prototyping of High-Resolution Large Format Microfluidic Device through Maskless Image Guided in-Situ Photopolymerization. *Nat Commun* **2023**, *14* (1). https://doi.org/10.1038/s41467-023-40119-x.

(2) Blevins, A. K.; Cox, L. M.; Hu, L.; Drisko, J. A.; Lin, H.; Bowman, C. N.; Killgore, J. P.; Ding, Y. Spatially Controlled Permeability and Stiffness in Photopatterned Two-Stage Reactive Polymer Films for Enhanced CO2 Barrier and Mechanical Toughness. *Macromolecules* **2021**, *54* (1), 44–52. https://doi.org/10.1021/acs.macromol.0c02355.

(3) Higgins, C. I.; Killgore, J. P.; DelRio, F. W.; Bryant, S. J.; McLeod, R. R. Photo-Tunable Hydrogel Mechanical Heterogeneity Informed by Predictive Transport Kinetics Model. *Soft Matter* **2020**, *16* (17), 4131–4141. https://doi.org/10.1039/d0sm00052c.

(4) Levalley, P. J.; Noren, B.; Kharkar, P. M.; Kloxin, A. M.; Gatlin, J. C.; Oakey, J. S. Fabrication of Functional Biomaterial Microstructures by in Situ Photopolymerization and Photodegradation. *ACS Biomater Sci Eng* **2018**, *4* (8), 3078–3087. https://doi.org/10.1021/acsbiomaterials.8b00350.

(5) Schwartz, J. J.; Boydston, A. J. Multimaterial Actinic Spatial Control 3D and 4D Printing. *Nat Commun* **2019**, *10* (1). https://doi.org/10.1038/s41467-019-08639-7.

(6) Rylski, A. K.; Maraliga, T.; Wu, Y.; Recker, E. A.; Arrowood, A. J.; Sanoja, G. E.; Page, Z. A. Digital Light Processing 3D Printing of Soft Semicrystalline Acrylates with Localized Shape

Memory and Stiffness Control. *ACS Appl Mater Interfaces* **2023**, *15* (28), 34097–34107. https://doi.org/10.1021/acsami.3c07172.

(7) Bagheri, A.; Jin, J. Photopolymerization in 3D Printing. *ACS Appl Polym Mater* **2019**, *1* (4), 593–611. https://doi.org/10.1021/acsapm.8b00165.

(8) Limberg, D. K.; Kang, J. H.; Hayward, R. C. Triplet-Triplet Annihilation Photopolymerization for High-Resolution 3D Printing. *J Am Chem Soc* **2022**, *144* (12), 5226–5232. https://doi.org/10.1021/jacs.1c11022.

(9) Rylski, A. K.; Cater, H. L.; Mason, K. S.; Allen, M. J.; Arrowood, A. J.; Freeman, B. D.; Sanoja, G. E.; Page, Z. A. Polymeric Multimaterials by Photochemical Patterning of Crystallinity. *Science (1979)* **2022**, *378* (6616), 211–215. https://doi.org/10.1126/science.add6975.

(10) Huh, J. T.; Moon, Y. W.; Park, J.; Atala, A.; Yoo, J. J.; Lee, S. J. Combinations of Photoinitiator and UV Absorber for Cell-Based Digital Light Processing (DLP) Bioprinting. *Biofabrication* **2021**, *13* (3). https://doi.org/10.1088/1758-5090/abfd7a.

(11) Saenz-Dominguez, I.; Tena, I.; Sarrionandia, M.; Torre, J.; Aurrekoetxea, J. An Analytical Model of Through-Thickness Photopolymerisation of Composites: Ultraviolet Light Transmission and Curing Kinetics. *Compos B Eng* **2020**, *191*. https://doi.org/10.1016/j.compositesb.2020.107963.

(12) O'Brien, A. K.; Bowman, C. N. Modeling Thermal and Optical Effects on Photopolymerization Systems. *Macromolecules* **2003**, *36* (20), 7777–7782. https://doi.org/10.1021/ma034070c.

(13) Camposeo, A.; Arkadii, A.; Romano, L.; D'Elia, F.; Fabbri, F.; Zussman, E.; Pisignano, D. Impact of Size Effects on Photopolymerization and Its Optical Monitoring In-Situ. *Addit Manuf* **2022**, *58*. https://doi.org/10.1016/j.addma.2022.103020.

(14) Courtecuisse, F.; Cerezo, J.; Croutxé-Barghorn, C.; Dietlin, C.; Allonas, X. Depth Characterization by Confocal Raman Microscopy of Oxygen Inhibition in Free Radical Photopolymerization of Acrylates: Contribution of the Thiol Chemistry. *J Polym Sci A Polym Chem* **2013**, *51* (3), 635–643. https://doi.org/10.1002/pola.26413.

(15) Fiedler, C. I.; Aisenbrey, E. A.; Wahlquist, J. A.; Heveran, C. M.; Ferguson, V. L.; Bryant, S. J.; McLeod, R. R. Enhanced Mechanical Properties of Photo-Clickable Thiol-Ene PEG Hydrogels through Repeated Photopolymerization of in-Swollen Macromer. *Soft Matter* **2016**, *12* (44), 9095–9104. https://doi.org/10.1039/c6sm01768a.

(16) Alketbi, A. S.; Shi, Y.; Li, H.; Raza, A.; Zhang, T. J. Impact of PEGDA Photopolymerization in Micro-Stereolithography on 3D Printed Hydrogel Structure and Swelling. *Soft Matter* **2021**, *17* (30), 7188–7195. https://doi.org/10.1039/d1sm00483b.

(17) Peterson, G. I.; Schwartz, J. J.; Zhang, D.; Weiss, B. M.; Ganter, M. A.; Storti, D. W.; Boydston, A. J. Production of Materials with Spatially-Controlled Cross-Link Density via Vat Photopolymerization. *ACS Appl Mater Interfaces* **2016**, *8* (42), 29037–29043. https://doi.org/10.1021/acsami.6b09768.

(18) Chan, J. W.; Shin, J.; Hoyle, C. E.; Bowman, C. N.; Lowe, A. B. Synthesis, Thiol-Yne "Click" Photopolymerization, and Physical Properties of Networks Derived from Novel Multifunctional Alkynes. *Macromolecules* **2010**, *43* (11), 4937–4942. https://doi.org/10.1021/ma1004452.

(19) Marklein, R. A.; Burdick, J. A. Spatially Controlled Hydrogel Mechanics to Modulate Stem Cell Interactions. *Soft Matter* **2009**, *6* (1), 136–143. https://doi.org/10.1039/b916933d.

(20) Fairbanks, B. D.; Scott, T. F.; Kloxin, C. J.; Anseth, K. S.; Bowman, C. N. Thiol-Yne Photopolymerizations: Novel Mechanism, Kinetics, and Step-Growth Formation of Highly Cross-Linked Networks. *Macromolecules* **2009**, *42* (1), 211–217. https://doi.org/10.1021/ma801903w.

(21) Wydra, J. W.; Cramer, N. B.; Stansbury, J. W.; Bowman, C. N. The Reciprocity Law Concerning Light Dose Relationships Applied to BisGMA/TEGDMA Photopolymers: Theoretical Analysis and Experimental Characterization. *Dental Materials* **2014**, *30* (6), 605–612. https://doi.org/10.1016/j.dental.2014.02.021.

(22) Mayerhöfer, T. G.; Mutschke, H.; Popp, J. Employing Theories Far beyond Their Limits—The Case of the (Boguer-) Beer–Lambert Law. *ChemPhysChem* **2016**, *17* (13), 1948–1955. https://doi.org/10.1002/cphc.201600114.

(23) Jacobs, P. F. *Rapid Prototyping & Manufacturing: Fundamentals of Stereolithography*; Society of Manufacturing Engineers, 1992.

(24) Uzcategui, A. C.; Muralidharan, A.; Ferguson, V. L.; Bryant, S. J.; McLeod, R. R. Understanding and Improving Mechanical Properties in 3D Printed Parts Using a Dual-Cure Acrylate-Based Resin for Stereolithography. *Adv Eng Mater* **2018**, *20* (12). https://doi.org/10.1002/adem.201800876.

(25) Lee, J. H.; Prud'homme, R. K.; Aksay, I. A. Cure Depth in Photopolymerization: Experiments and Theory. *J Mater Res* **2001**, *16* (12), 3536–3544. https://doi.org/10.1557/JMR.2001.0485.

(26) Kolibaba, T. J.; Killgore, J. P.; Caplins, B. W.; Higgins, C. I.; Arp, U.; Miller, C. C.; Poster, D. L.; Zong, Y.; Broce, S.; Wang, T.; Talačka, V.; Andersson, J.; Davenport, A.; Panzer, M. A.; Tumbleston, J. R.; Gonzalez, J. M.; Huffstetler, J.; Lund, B. R.; Billerbeck, K.; Clay, A. M.; Fratarcangeli, M. R.; Qi, H. J.; Porcincula, D. H.; Bezek, L. B.; Kikuta, K.; Pearlson, M. N.; Walker, D. A.; Long, C. J.; Hasa, E.; Aguirre-Soto, A.; Celis-Guzman, A.; Backman, D. E.; Sridhar, R. L.; Cavicchi, K. A.; Viereckl, R. J.; Tong, E.; Hansen, C. J.; Shah, D. M.; Kinane, C.; Pena-Francesch, A.; Antonini, C.; Chaudhary, R.; Muraca, G.; Bensouda, Y.; Zhang, Y.; Zhao, X. Results of an Interlaboratory Study on the Working Curve in Vat Photopolymerization. *Addit Manuf* **2024**, *84*. https://doi.org/10.1016/j.addma.2024.104082.

(27) Miller, G. A.; Gou, L.; Narayanan, V.; Scranton, A. B. Modeling of Photobleaching for the Photoinitiation of Thick Polymerization Systems. *J Polym Sci Part A: Polym Chem* **2002**, *40* (6), 793–808. https://doi.org/10.1002/pola.10162.

(28) Rusu, M. C.; Block, C.; Van Assche, G.; Van Mele, B. Influence of Temperature and UV Intensity on Photo-Polymerization Reaction Studied by Photo-DSC. *J Therm Anal Calorim* **2012**, *110* (1), 287–294. https://doi.org/10.1007/s10973-012-2465-5.

(29) Golaz, B.; Michaud, V.; Leterrier, Y.; Mnson, J. A. E. UV Intensity, Temperature and Dark-Curing Effects in Cationic Photo-Polymerization of a Cycloaliphatic Epoxy Resin. *Polymer (Guildf)* **2012**, *53* (10), 2038–2048. https://doi.org/10.1016/j.polymer.2012.03.025.

(30) Cox, L. M.; Blevins, A. K.; Drisko, J. A.; Qi, Y.; Ding, Y.; Fiedler-, C. I.; Long, R.; Bowman, C. N.; Killgore, J. P.; Cox, L. M.; Killgore, J. P. Tunable Mechanical Anisotropy, Crack Guiding, and Toughness Enhancement in Two- Stage Reactive Polymer Networks. *Adv Eng Mater* **2019**, *21* (8). https://doi.org/10.1002/adem.201900578.

(31) Nair, D. P.; Podgórski, M.; Chatani, S.; Gong, T.; Xi, W.; Fenoli, C. R.; Bowman, C. N. The Thiol-Michael Addition Click Reaction: A Powerful and Widely Used Tool in Materials Chemistry. *Chem Mater* **2014**, *26* (1), 724–744. https://doi.org/10.1021/cm402180t.

(32) Nair, D. P.; Cramer, N. B.; McBride, M. K.; Gaipa, J. C.; Shandas, R.; Bowman, C. N. Enhanced Two-Stage Reactive Polymer Network Forming Systems. *Polymer (Guildf)* **2012**, *53* (12), 2429–2434. https://doi.org/10.1016/j.polymer.2012.04.007.

(33) O'Brien, A. K.; Cramer, N. B.; Bowman, C. N. Oxygen Inhibition in Thiol-Acrylate Photopolymerizations. *J Polym Sci A Polym Chem* **2006**, *44* (6), 2007–2014. https://doi.org/10.1002/pola.21304.

(34) Cramer, N. B.; O'Brien, C. P.; Bowman, C. N. Mechanisms, Polymerization Rate Scaling, and Oxygen Inhibition with an Ultra-Rapid Monovinyl Urethane Acrylate. *Polymer (Guildf)* **2008**, *49* (22), 4756–4761. https://doi.org/10.1016/j.polymer.2008.08.051.

(35) Kwisnek, L.; Nazarenko, S.; Hoyle, C. E. Oxygen Transport Properties of Thiol-Ene Networks. *Macromolecules* **2009**, *42* (18), 7031–7041. https://doi.org/10.1021/ma901117s.

(36) Kwisnek, L.; Kaushik, M.; Hoyle, C. E.; Nazarenko, S. Free Volume, Transport, and Physical Properties of n-Alkyl Derivatized Thiol-Ene Networks: Chain Length Effect. *Macromolecules* **2010**, *43* (8), 3859–3867. https://doi.org/10.1021/ma1001113.

(37) Kwisnek, L.; Goetz, J.; Meyers, K. P.; Heinz, S. R.; Wiggins, J. S.; Nazarenko, S. PEG Containing Thiol-Ene Network Membranes for CO2 Separation: Effect of Cross-Linking on Thermal, Mechanical, and Gas Transport Properties. *Macromolecules* **2014**, *47* (10), 3243–3253. https://doi.org/10.1021/ma5005327.

(38) Blevins, A. K.; Hu, L.; Azad, A. A.; Cox, L. M.; Killgore, J. P.; Lin, H.; Ding, Y. Impact of Interfaces on the CO2 Permeability of Photopatterned Two-Stage Thiolene Polymer Films. *Macromolecules* **2023**, *57* (3), 1354–1361. https://doi.org/10.1021/acs.macromol.3c01987.

(39) Kwisnek, L.; Heinz, S.; Wiggins, J. S.; Nazarenko, S. Multifunctional Thiols as Additives in UV-Cured PEG-Diacrylate Membranes for CO2 Separation. *J Memb Sci* **2011**, *369* (1–2), 429–436. https://doi.org/10.1016/j.memsci.2010.12.022.

(40) Asvany, O.; Yamada, K. M. T.; Brünken, S.; Potapov, A.; Schlemmer, S. Experimental Ground-State Combination Differences of CH5+. *Science (1979)* **2015**, *347* (6228), 1346–1348. https://doi.org/10.1126/science.aaa3304.

(41) Taki, K. A Simplified 2D Numerical Simulation of Photopolymerization Kinetics and Oxygen Diffusion-Reaction for the Continuous Liquid Interface Production (CLIP) System. *Polymers (Basel)* **2020**, *12* (4). https://doi.org/10.3390/polym12040875.

(42) Kim, D. S. (Danny); Suriboot, J.; Grunlan, M. A.; Tai, B. L. Feasibility Study of Silicone Stereolithography with an Optically Created Dead Zone. *Addit Manuf* **2019**, *29*. https://doi.org/10.1016/j.addma.2019.100793.

(43) Li, Y.; Mao, Q.; Yin, J.; Wang, Y.; Fu, J.; Huang, Y. Theoretical Prediction and Experimental Validation of the Digital Light Processing (DLP) Working Curve for Photocurable Materials. *Addit Manuf* **2021**, *37*. https://doi.org/10.1016/j.addma.2020.101716.

(44) Terrones, G.; Pearlstein, A. J. Effects of Optical Attenuation and Consumption of a Photobleaching Initiator on Local Initiation Rates in Photopolymerizations. *Macromolecules* **2001**, *34* (10), 3195–3204. https://doi.org/10.1021/ma001235y.

(45) Mucci, V.; Vallo, C. Efficiency of 2,2-Dimethoxy-2-Phenylacetophenone for the Photopolymerization of Methacrylate Monomers in Thick Sections. *J Appl Polym Sci* **2012**, *123* (1), 418–425. https://doi.org/10.1002/app.34473.

(46) Cramer, N. B.; Reddy, S. K.; Cole, M.; Hoyle, C.; Bowman, C. N. Initiation and Kinetics of Thiol-Ene Photopolymerizations without Photoinitiators. *J Polym Sci A Polym Chem* **2004**, *42* (22), 5817–5826. https://doi.org/10.1002/pola.20419.

(47) Hoyle, C. E.; Lee, T. Y.; Roper, T. Thiol-Enes: Chemistry of the Past with Promise for the Future. *J Polym Sci A Polym Chem* **2004**, *42* (21), 5301–5338. https://doi.org/10.1002/pola.20366.

(48) Kumar, R.; Kaura, S. K.; Sharma, A. K.; Chhachhia, D. P.; Aggarwal, A. K. Knife-Edge Diffraction Pattern as an Interference Phenomenon: An Experimental Reality. *Opt Laser Technol* **2007**, *39* (2), 256–261. https://doi.org/10.1016/j.optlastec.2005.08.008.

(49) Santhanakrishnan, T.; Rajesh, R.; Awasthi, R. L.; Sreehari, C. V. Optical Diffraction Phenomena around the Edges of Photodetectors: A Simplified Method for Metrological Applications. *Sci Rep* **2019**, *9* (1). https://doi.org/10.1038/s41598-019-40270-w.

(50) Cheng, Y.; Lin, C. Y.; Wei, D. H.; Loechel, B.; Gruetzner, G. Wall Profile of Thick Photoresist Generated via Contact Printing. *Journal of Microelectromechanical Systems* **1999**, *8* (1), 18–26. https://doi.org/10.1109/84.749398.

(51) Wu, D.; Zhao, Z.; Zhang, Q.; Qi, H. J.; Fang, D. Mechanics of Shape Distortion of DLP 3D Printed Structures during UV Post-Curing. *Soft Matter* **2019**, *15* (30), 6151–6159. https://doi.org/10.1039/c9sm00725c.

(52) Li, Y.; Mao, Q.; Li, X.; Yin, J.; Wang, Y.; Fu, J.; Huang, Y. High-Fidelity and High-Efficiency Additive Manufacturing Using Tunable Pre-Curing Digital Light Processing. *Addit Manuf* **2019**, *30*. https://doi.org/10.1016/j.addma.2019.100889.

(53) Darabi, A.; Long, R.; Weber, J. C.; Cox, L. M. Effect of Geometry and Orientation on the Tensile Properties and Failure Mechanisms of Compliant Suture Joints. *ACS Appl Mater Interfaces* **2023**, *15* (8), 11084–11091. https://doi.org/10.1021/acsami.2c21925.

Table of Contents